Earth and Planetary Science Letters 455 (2016) 14–24

Contents lists available at ScienceDirect

Earth and Planetary Science Letters

www.elsevier.com/locate/epsl

Exploration of remote triggering: A survey of multiple fault structures in Haiti

Chastity Aiken [a,b,*,1], Kevin Chao [c], Hector Gonzalez-Huizar [d], Roby Douilly [e,2], Zhigang Peng [a], Anne Deschamps [f], Eric Calais [g], Jennifer S. Haase [h]

[a] Georgia Institute of Technology, School of Earth and Atmospheric Sciences, Atlanta, GA, United States
[b] University of Texas at Austin, Institute for Geophysics, Austin, TX, United States
[c] Center for Optimization and Statistical Learning, Northwestern Institute on Complex Systems, Northwestern University, Evanston, IL, United States
[d] University of Texas at El Paso, Department of Geological Sciences, El Paso, TX, United States
[e] Purdue University, Department of Earth, Atmospheric, and Planetary Sciences, West Lafayette, IN, United States
[f] Université Côte d'Azur, CNRZ, OCA, IRD, Géoazur, Nice, France
[g] Ecole Normale Supérieure, Department of Géosciences, PSL Research University, Paris, France
[h] University of California, Institute of Geophysics and Planetary Physics, San Diego, CA, United States

ARTICLE INFO

Article history:
Received 28 February 2016
Received in revised form 15 August 2016
Accepted 13 September 2016
Available online 4 October 2016
Editor: B. Buffett

Keywords:
tremor
aftershocks
Haiti
triggering
matched filter detection

ABSTRACT

Triggering studies provide an important tool for understanding the fundamental physics of how faults slip and interact, and they also provide clues about the stress states of faults. In this study, we explore how seismic waves from the 27 February 2010 *Mw*8.8 Maule, Chile mainshock interact with the left lateral strike-slip Enriquillo–Plantain Garden Fault (EPGF) and surrounding reverse faults in the southern Haiti peninsula. The Chile mainshock occurred 6,000 km away and just 46 days after the 12 January 2010 *Mw*7.0 Haiti earthquake, a tragic event which activated multiple faults in the southern Haiti peninsula. During the surface waves of the Chile mainshock, several tectonic tremor signals were observed, originating from south of the EPGF trace. Cross-correlation of the triggered tremor and transient stresses resolved onto to the EPGF indicates that the Love wave of the Chile mainshock was the primary driving mechanism of the triggered deep shear slip and tremor signals, as opposed to dilatational stress changes generated by the Rayleigh wave. We also searched for any influence of transient stresses on Haiti aftershock activity by applying the matched filter technique to multiple days of seismic data around the time of the Chile mainshock. While we identified a slight increase in Haiti aftershock activity rate, the rate changes were significant only when small magnitude events were included in the significance tests. These observations are generally consistent with recent inferences that deep tectonic tremor is more sensitive than shallow earthquakes to external stress perturbations.

1. Introduction

Seismic activity, such as earthquakes or tectonic tremor, naturally occurs on active fault systems due to tectonic stressing between plate boundaries. While earthquakes mostly occur in the brittle upper crust, deep tectonic tremor (Obara, 2002) is found in the lower crust along major plate-boundary faults, at times accompanying geodetically recorded slow-slip events (*e.g.*, Beroza and Ide, 2011). Sometimes tremor and earthquakes can be triggered by transient stress changes associated with the passing seismic waves of earthquakes (*e.g.*, Peng and Gomberg, 2010; Hill and Prejean, 2015). This process of fault failure induced by seismic waves is commonly known as 'dynamic triggering' and has been observed worldwide in a wide range of tectonic environments (*e.g.*, Brodsky and Prejean, 2005; Velasco et al., 2008; Peng and Gomberg, 2010; Hill and Prejean, 2015). Because seismic waves of distant earthquakes are capable of inducing fault failure, triggering studies can be used as a probe to not only understand a fault's current state of stress but to also better understand how seismic activity occurs on active fault systems and how faults interact with one another (Brodsky and van der Elst, 2014).

Dynamic triggering generally occurs when transient stresses act in the same direction as a fault's natural motion, *i.e.* dynamic Coulomb stress increases (Hill, 2012), but dynamic triggering can

* Corresponding author at: University of Texas at Austin, Institute for Geophysics, J.J. Pickle Research Campus, Bldg. 196, 10100 Burnet Rd. (R2200), Austin, TX 78758-4445, United States.
E-mail address: caiken@ig.utexas.edu (C. Aiken).
[1] Now at University of Texas at Austin, Institute for Geophysics.
[2] Now at University of California, Riverside, Department of Earth Sciences.

http://dx.doi.org/10.1016/j.epsl.2016.09.023
0012-821X/

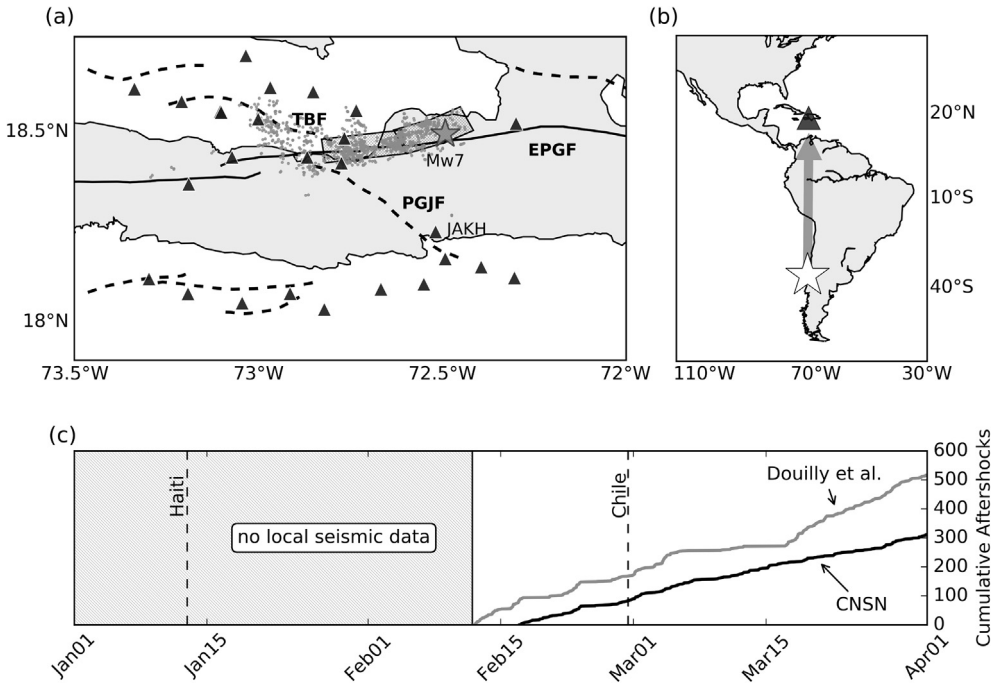

Fig. 1. Southern Haiti study region and local seismicity. (a) Left-lateral strike-slip Enriquillo–Plantain Garden Fault (EPGF, solid black line) marks the boundary between the Caribbean Plate to the south and Gonâve microplate to the north and is surrounded by several reverse faults (dashed lines), including the Trois Baies Fault (TBF) and Petit Goave–Jacmel Fault (PGJF). Triangles mark seismic stations used in this study. The 12 January 2010 *Mw*7.0 Haiti mainshock (gray star) and its aftershocks (gray dots) occur mostly north of the EPGF. Hatched area marks the east and west fault plane of the Léogâne Fault delineated from aftershock locations (Douilly et al., 2013). (b) Location of the 27 February 2010 *Mw*8.8 Maule, Chile earthquake (white star) and Haiti region (triangle). Arrow marks seismic wave propagation direction (almost perpendicular to EPGF). (c) Haiti aftershocks from the Canadian National Seismograph Network (CNSN) and Douilly et al. (2013). Haiti and Chile mainshocks occurred 46 days apart.

also occur as a result of secondary stress transfer (*e.g.*, Hill and Prejean, 2015). One example of secondary transfer is movement of fluids that exist in Earth's crust by passing seismic waves (*e.g.* Brodsky et al., 2003; Brodsky and Prejean, 2005). Essentially, seismic waves can pressurize fluids in Earth's crust, which may unclamp a fault if great enough and thereby reduces a fault's normal stress and promotes failure, according to the Coulomb failure model (Hill, 2012). Such a secondary triggering process is thought to be responsible for the observation of dynamically triggered earthquakes in extensional and transtensional regions (geothermal and volcanic regions) with ample fluids (*e.g.*, Prejean et al., 2004; Hill and Prejean, 2015). High fluid pressure is also thought to be a contributing factor for the dynamic triggering of tectonic tremor in compressional regions (subduction zones) (Peng and Gomberg, 2010; Beroza and Ide, 2011) and transpressional regions such as the San Andreas Fault in California (Hill et al., 2013; Peng et al., 2015) and the Oriente Fault in Cuba (Peng et al., 2013), as well as the Queen Charlotte Fault and Eastern Denali Fault in western Canada (Aiken et al., 2013, 2015).

In this study, we explore dynamic triggering in the southern Haiti peninsula region (Fig. 1). This region experienced a 240-year quiescence of moderate-size and larger earthquakes until 12 January 2010 when a *Mw*7.0 Haiti earthquake occurred (Bakun et al., 2012). Prior to the 2010 Haiti earthquake, no research quality stations were in operation in the region. The Haiti earthquake prompted many institutions to deploy temporary and permanent seismic stations surrounding the plate-bounding Enriquillo–Plantain Garden Fault (EPGF), both on land and offshore (Fig. 1a) to record aftershock activity (*e.g.*, Mercier de Lépinay et al., 2011). Aftershock activity delineated a previously unmapped north-dipping transpressional fault north of the EPGF as the source of the Haiti earthquake (now known as the Léogâne Fault). Due to static stress transfer, aftershocks also occurred on the reverse Trois Baies Fault (TBF) and transpressional EPGF (Douilly et al., 2013). It is worth noting that aftershock zones are known to be susceptible to triggering (*e.g.*, Hough el al., 2003; Jiang et al., 2010) due to their critically stressed state attributed to stress changes caused by the mainshock.

Forty-six days after the Haiti earthquake, the 27 February 2010 *Mw*8.8 Maule, Chile earthquake occurred about 6,000 km away from Haiti (Fig. 1b). The Chile earthquake is the 6th largest earthquake that has occurred since 1900, and its surface waves have triggered microearthquakes and tremor in many regions of the Western Hemisphere (*e.g.*, Fry et al., 2011; Zigone et al., 2012; Peng et al., 2011, 2013; Gomberg and Prejean, 2013; Aiken et al., 2013, 2015; Aiken and Peng, 2014), as well as icequakes in Antarctica (Peng et al., 2014). Because of its widespread triggering and because the southern Haiti region was in a critically stressed state, we investigate here whether the Chile mainshock triggered earthquakes and/or tectonic tremor on faults activated by the Haiti earthquake in the southern Haiti peninsula region. Such an investigation provides an opportunity to better understand how multiple fault structures that are critically stressed respond to external stress perturbations.

2. Search for dynamic triggering of tremor

2.1. General observations

Amidst the ongoing aftershock activity of the Haiti mainshock, we found tremor signals triggered during the Love and Rayleigh (surface) waves of the Chile earthquake (Fig. 2), though no similar signals were observed in the few days before the Chile earthquake. Three distinct tremor-like signals containing frequencies of ~1–10 Hz are clearly visible, coincident with the first few cycles of the Love waves. These tremor signals are easily distinguished from the on-going aftershock activity, since the tremor bursts are emergent signals without distinct *P*- or *S*-waves (Fig. 2b) and have a longer duration compared to small, local aftershocks (Fig. 2c). Though the tremor signals are visibly different from the local after-

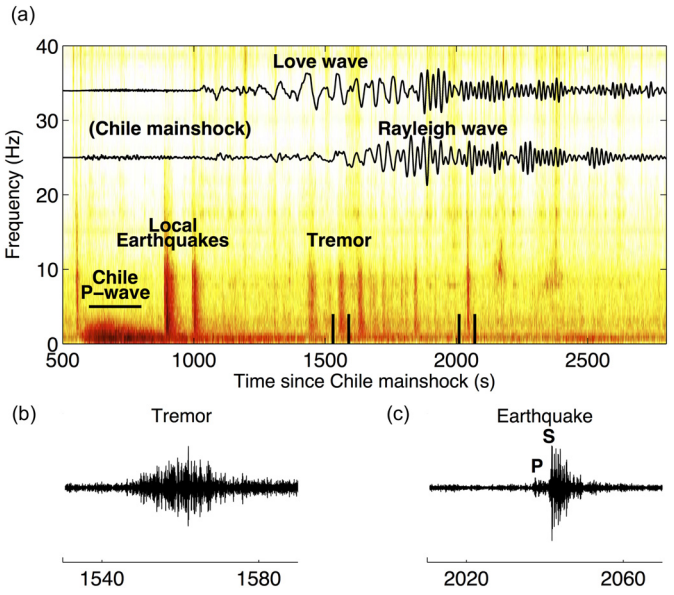

Fig. 2. (a) Spectra of tremor triggered by the Maule, Chile earthquake and Haiti aftershocks recorded at station JAKH (see Fig. 1). There is a strong correlation between the first few cycles of the Love wave and 3 strong tremor bursts. (b–c) Example of a tremor burst that lacks distinct seismic wave arrivals (emergent) and an aftershock having distinct (impulsive) *P*- and *S*-waves. Times for these events are marked in (a) by vertical black bars.

shocks, they do look similar to *P*-waves of earthquakes occurring at regional and remote distances. The Advanced National Seismograph System (ANSS) reported 3 $M \geq 5.6$ Chile aftershocks occurring during the time that the Chile mainshock's surface waves arrive in the Haiti region. When predicting the *P*-wave arrivals of these aftershocks, we found that 2 of the 3 aftershocks do not correlate with any tremor burst arrivals while one aftershock *P*-wave arrival seemingly correlates (Fig. 3). However, the *P*-wave amplitude and frequency contents of these aftershocks that seemingly correlate should be lower than that of the Chile mainshock and the tremor (Fig. 2). Furthermore, we found that these tremor-like signals propagate in space and time with a shear wave speed of $\sim$3.5 km s^{-1} (Fig. S1). These observations are similar to tremor observations at other plate-boundary regions (*e.g.*, Peng and Gomberg, 2010; Chao et al., 2013). In addition, after speeding up 100 times (Kilb et al., 2012; Peng et al., 2012), the tremor signals (Movie S1) are audibly different (start of steam engine) compared to the *P*-wave of the Chile mainshock (distant thunder) and local Haiti aftershocks (firecrackers).

2.2. Location of tremor sources

The 3 tremor signals shown in Fig. 2 are observable on all 25 seismic stations (6 on land, 19 offshore) in the southern Haiti peninsula after applying a 2–16 Hz band-pass filter (Fig. 3, dark arrows). Such a filter enhances local seismic signals and mostly suppresses the teleseismic body wave coda (*P*- and *S*-waves) of the remote Chile mainshock and its early aftershocks. In the 2–16 Hz frequency band, there are a few interspersed tremors between the three strong tremors (white arrows), but they are weaker and hardly visible (if at all) in the spectrogram (Fig. 2). In total, $\sim$10 tremor bursts appear to be triggered by the surface waves of the Chile mainshock (Fig. 3).

We located the tremor bursts using an envelope cross-correlation technique (*e.g.*, Chao et al., 2013; Chao and Obara, 2016). This method searches a 3D grid for the minimum differential times between arrivals on station pairs and theoretical travel times using a local velocity model (Table S1). Prior to locating the tremor, we applied corrections to all stations to account for travel time delays through thick sediments of the ocean basins and other near surface effects, similar to Douilly et al. (2013) (Table S2).

Table 1
Horizontal locations and associated errors for 9 tremor bursts.[a]

Burst No.	Longitude	Error (+/−)	Latitude	Error (+/−)
1	−72.6675°	0.0442°	18.3592°	0.0500°
2	−72.8233°	0.1096°	18.2450°	0.1133°
3	−72.8233°	0.0446°	18.3117°	0.0483°
4	−72.7742°	0.0467°	18.2433°	0.0504°
5	−72.8208°	0.0127°	18.3531°	0.0150°
6	−72.8092°	0.0221°	18.2592°	0.0279°
7	−72.6383°	0.0375°	18.3792°	0.0408°
8	−72.7292°	0.0625°	18.2133°	0.0729°
10	−72.7792°	0.0521°	18.3225°	0.0517°

[a] Errors determined from bootstrapping methods by dropping one station for each grid search run. The depths are set to 25 ± 5 km, as constrained by burst #5.

Because the tremor bursts were not observable on all 25 seismic stations, we computed all possible station combinations using different numbers of stations (10 to 25) and finally selected a set of 13 stations that provided a stable location (station names with $*$ in Fig. 3). For these 13 stations, we utilized a bootstrapping method such that when one station was dropped, the grid search for the best fitting location was performed. Thus, each tremor burst was located 14 times, once when using all 13 stations and once for each station dropped. Horizontal locations outside one standard deviation (1σ) were rejected, and the final location was computed as the average of the locations within 1σ (*e.g.*, Fig. S2). We tested this method using 15 stations (Fig. S3), but the 13-station set gave smaller horizontal errors and more stable results. When the 13 stations were used to locate the triggered tremor sources, we obtained an average tremor depth of $\sim$25 km for burst #5, the largest amplitude tremor triggered by the Chile mainshock (Figs. 3 and S2). This depth is similar to previous observations of tremor occurrence on strike-slip faults (*e.g.*, Shelly et al., 2009) and much deeper than that of relocated aftershocks (Fig. 4). We were not able to constrain the depths for the other tremor sources, and so we set their depths to be 25 km, similar to that of burst #5. We note that while most aftershocks occurred north of the EPGF, the 9 locatable tremors originated from south of the EPGF (Fig. 4). These locations remain essentially unchanged if we use different sets of stations in the location procedure, such as when 2 stations are added to the location procedure (*e.g.*, Fig. S3). Table 1 summarizes the horizontal locations and associated errors for the 9 tremor bursts.

2.3. Coulomb triggering potential

2.3.1. Surface wave stresses

As the surface waves of the Chile mainshock passed through the southern Haiti peninsula, they induced transient stress changes. Here, we modeled how these transient stresses behave at the tremor source on a plane oriented similar to the EPGF. In practice, this model of transient stresses caused by surface waves is defined as the 'triggering potential' of the surface waves (*e.g.*, Hill, 2012). Triggering potential is a measure of the change in Coulomb failure stress (δCFF, also known as Coulomb failure function) on a fault plane and is estimated from the change in shear ($\delta\tau$) and normal ($\delta\sigma_n$) stresses on a fault plane induced from the passing waves, such that

$$\delta CFF = \delta\tau + \mu\delta\sigma_n \quad (1)$$

where μ is the coefficient of friction on the fault plane. This model accounts for fault geometry, amplitude and dominant frequency of the passing waves, and location (longitude, latitude, and depth) of the triggered source. Gonzalez-Huizar and Velasco (2011) provided a full description of how to compute changes in the Coulomb

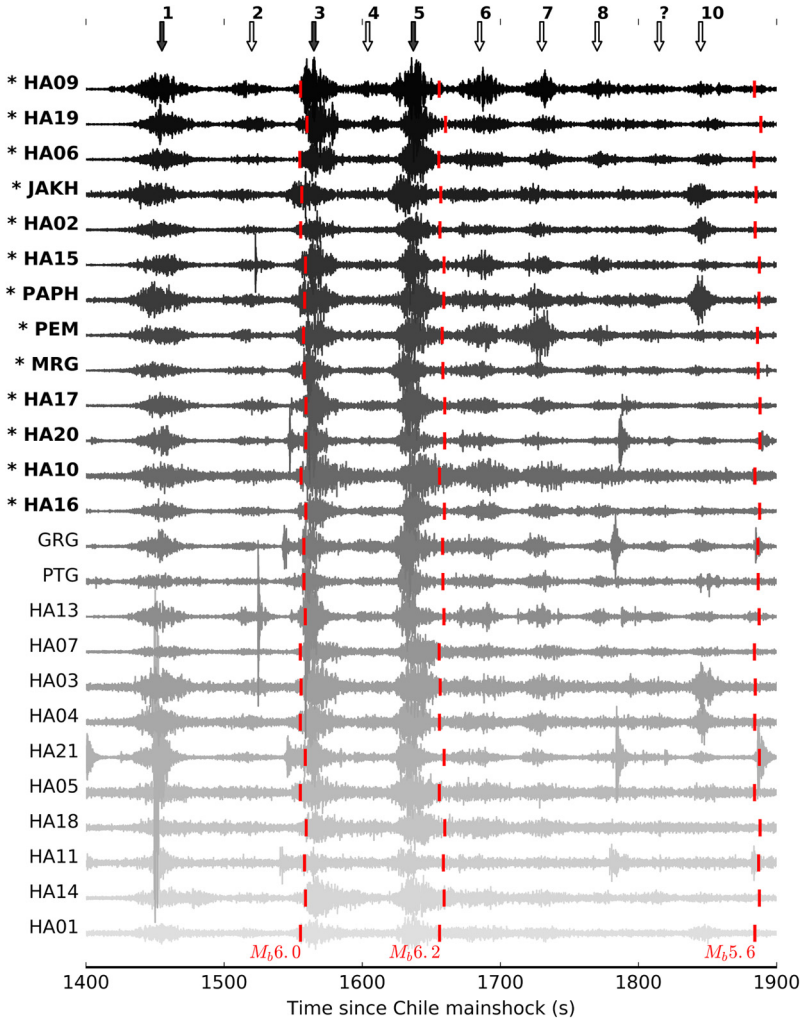

Fig. 3. Tremor bursts triggered by the surface waves of the Chile mainshock as recorded on 25 seismic stations (6 on land; 19 offshore). Waveforms are filtered to the 2–16 Hz frequency band. Strong tremor signals (see Fig. 2) are marked with dark arrows. Weak tremor signals are marked by light arrows. Each tremor burst is assigned a number according to its occurrence in time since the Chile mainshock. The *P*-wave arrival times of 3 large aftershocks from the Chile region (predicted using *TauP*) are marked with vertical red lines. We also note their body-wave magnitudes (M_b). Starred station names mark those utilized in the envelope cross-correlation method for tremor source location. Some low magnitude aftershocks with large amplitude, impulsive arrivals are also visible on a few stations.

failure function from broadband seismograms, and we briefly summarize the method here.

First, waveforms from station JAKH were time-shifted to the average location of the 9 tremor burst sources using a local velocity model (Table S1), assuming a tremor source depth of 25 km. We measured the triggering wave's amplitude and frequency from consecutive peaks in the displacement seismograms and then computed the dynamic stress tensor for those peak values and interpolated them to obtain time-dependent components of stress tensors. Next, we rotated the time-dependent stress tensor to the orientation of the EPGF (E–W strike $= 0°$, vertical dip $= 90°$). Then, the changes in shear ($\delta\tau$) and normal ($\delta\sigma_n$) stress were calculated, which are used to estimate the Coulomb failure stress δCFF as defined in equation (1). Based on Thomas et al. (2009) and Houston (2015), we select a coefficient of friction (μ) of 0.1 for the stress modeling at tremor depths. Modeled stress changes are presented as a function of time in what we define as 'stressgrams' (Fig. 5).

The total stress change is calculated as the sum of the stress changes caused by the Rayleigh and the Love waves of the Chile mainshock. For the EPGF, stress changes caused by the Love wave of the Chile mainshock are much greater than the stress changes caused by the Rayleigh wave. Therefore, the 'stressgram' of the total stress shows almost no difference from the Love wave 'stressgram' (Fig. 5). When the tremor envelope function was cross-correlated with the Love and Rayleigh 'stressgrams' computed at the average tremor burst location, we obtained cross-correlation (CC) values of 0.94 and −0.07, respectively (Table 2). One may also notice the trace of the Petit Goave–Jacmel Fault (PGJF), a south-dipping reverse fault, divides the tremor source locations and could also be a likely faulting source for the triggered tremor (Fig. 4). The geometry of the PGJF is not well studied, but it is reasonable to assume that it has a dip similar to the Trois Baies Fault, which has a similar strike to the PGJF but lies north of the EPGF. The Trois Baies Fault is known to have a dip of 45° based on the relocation of aftershocks (Douilly et al., 2013). Therefore, for PGJF 'stressgram' calculations we used a strike of 125° and a dip of 45°S. Similar to the EPGF, the modeling suggests that Love wave stress changes on the PGJF were much greater than those caused by the Rayleigh wave of the Chile mainshock. Furthermore, given this orientation for the PGJF, the Love and Rayleigh waves of the Chile mainshock have smaller stress changes than those resolved on the EPGF (Fig. 5) and, when cross-correlated with the tremor envelope, also have lower CC values of 0.71 and −0.01 for the Love and Rayleigh waves, respectively, at the average tremor source location (Table 2). While the Love wave 'stressgrams' indicate that the tremor could be triggered by the Love wave of the Chile mainshock

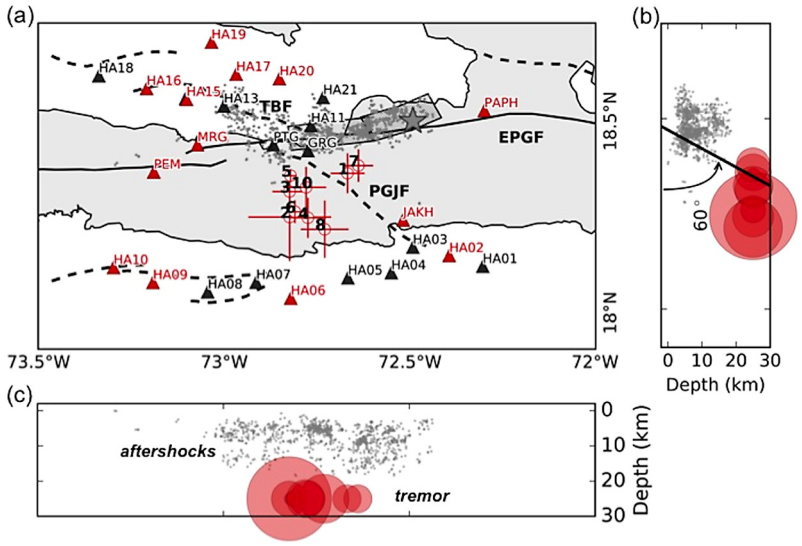

Fig. 4. (a) Local aftershocks (gray dots) and triggered tremor burst (circles) hypocenters. Crosshairs indicate location errors. Seismic stations used for tremor burst location are shown in red. Tremor bursts are numbered in order of occurrence, as in Fig. 3. Other notations and symbols are similar to Fig. 1a. (b) Depth profile in the N–S direction with a high-angle EPGF depicted. (c) Depth profile in the E–W direction. Tremor sources mostly originate from south of the EPGF trace with no apparent migration. Table 1 lists tremor locations and errors. Tremor (circles) sources are translucently plotted red in (b) and (c) to show overlapping locations. Tremor symbol size solely reflects latitude and longitude location errors in (b) and (c), respectively. There is no vertical exaggeration in (b) and (c).

Table 2
Tremor envelope and 'stressgram' cross-correlation (CC) results.

Test No.	Location of stress calculation	CC time (s)[a]	Surface wave	Normed CC	
				EPGF	*PGJF*
1	9-burst average	1400 to 1900	Love	0.94	0.71
			Rayleigh	−0.07	−0.01
2	burst #5	1400 to 1900	Love	0.96	0.75
			Rayleigh	0.02	−0.03
3	burst #5	1610 to 1650	Love	0.21	0.17
			Rayleigh	−0.04	0.04

[a] Time since Chile mainshock.

on either the PGJF or the EPGF (CC = 0.71 and 0.94, respectively), the tremor is more likely occurring on the EPGF because the degree of correlation between the average tremor location and the resolved stresses at the average tremor location is higher. In addition, the Love wave applied greater stress on the EPGF (∼10 kPa) compared to the PGJF (∼2 kPa). Hence, tremor was more likely triggered on the EPGF.

We note that in this study we did not account for the one-sided nature of the tremor envelope when cross-correlating it with 'stressgrams' that have zero mean. Here, we utilized only the positive stress, which is known to trigger tremor (Hill, 2012). When the stress is negative, the fault will not slip and only background noise is recorded. Tremor envelopes are also utilized for locating tremor sources, as noted in the previous section. Therefore, we are confident that cross-correlating a one-sided tremor envelope with a zero mean 'stressgram' does not omit information about how the triggering occurred.

Because not all tremor bursts occur at the average tremor burst location, we also tested how the CC values vary when CC time windows and location of the computed 'stressgram' are changed. Specifically, we tested the variation of the CC value at burst #5 location (our best location) and time for the EPGF and PGJF (Table 2, tests 2–3). Although changing the size of the time window affects the CC, in all cases the Love wave stresses shows a higher CC than Raleigh wave stresses when resolved onto the EPGF. The high temporal correlation of the tremor bursts with the Love wave for the EPGF suggest that, in this case, the Love wave is responsible for triggering tremor, likely on the deep extension of the EPGF.

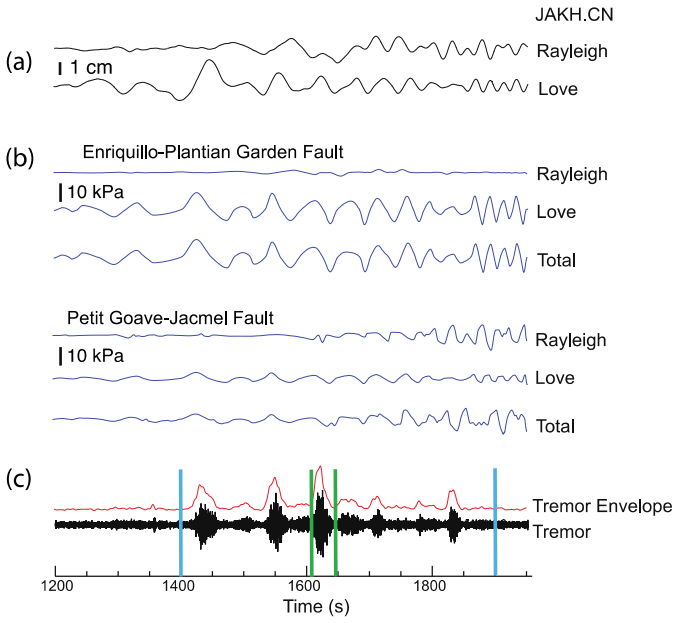

Fig. 5. Correlations between dynamic stresses of surface waves from the Chile mainshock and tremor activity. (a) Broadband vertical and transverse displacement waveforms from station JAKH. (b) Computed dynamic 'stressgrams' for the surface waves resolved onto the EPGF and PGJF. (c) Band-pass filtered 2–16 Hz waveform showing tremor and its envelope function. Surface wave window (blue bars) and burst #5 window (green bars) mark the times for cross-correlation tests indicated in Table 2.

In terms of resolving the surface wave triggering potential (equation (1)), the coefficient of friction μ represents the fraction of normal stress changes ($\delta\sigma_n$) that contributes to dynamic Coulomb stress changes (δCFF). The coefficient of friction value μ used in previous studies is typically around 0.4 for calculations of static Coulomb stress changes (*e.g.*, Toda et al., 2011). However, it has been shown that μ at lower crustal depths where tremor occurs can range from 0 to 0.15 (Thomas et al., 2009; Houston, 2015). In this study, we utilized $\mu = 0.1$ for our stress modeling, but we also calculated the surface waves related stress ('stressgrams') us-

ing different values of μ (Tables S4–S5). Regardless the value of μ, the Love wave causes almost no change to the normal stress component ($\delta\sigma_n$) on a fault plane oriented perpendicularly to the direction of wave propagation (Gonzalez-Huizar and Velasco, 2011; Hill, 2012). In addition, the amplitude of the Rayleigh wave was much lower than the amplitude of the Love wave of the Chile mainshock (Fig. 5), resulting in a significantly small $\delta\sigma_n$ compared with $\delta\tau$. Therefore, given the very low $\delta\sigma_n$, we observed no significant change in the modeled δCFF ('stressgrams') for different values of μ for either the EPGF or the PGJF (Tables S4–S5).

2.3.2. Test of fault orientation

The structures of many faults in the southern Haiti peninsula were not well studied until the 2010 *Mw*7.0 Haiti earthquake. No clear evidence of surface ruptures were observed on the EPGF following the Haiti earthquake (Prentice et al., 2010), consistent with other observations that it originated on a north-dipping blind-reverse fault (Calais et al., 2010). Field observations instead suggested that the EPGF is a vertical to high-angle (>60°) south-dipping structure (Prentice et al., 2010).

Given the incidence of the Love wave on the EPGF (Fig. 1b), the Coulomb triggering potential predicts triggering solely by the Love wave (Hill, 2012). In other words, the cross-correlation of the Love wave 'stressgram' and tremor envelope should be close to 1 at some fault dip angle. Hence we can search for the best-fitting dip of the EPGF that gives the highest CC value. To do so, we varied the dip of the EPGF in our triggering potential model between 0° and 90° and cross-correlated the computed 'stressgram' and tremor envelope for each dip. For the EPGF, CC values for the Love wave 'stressgram' and tremor envelope occurs when the dip of the fault increases (Fig. 6a), for different locations and CC time windows (see Table 2). In addition, the cross-correlation values do not vary much when computing the 'stressgram' for the entire surface wave window at different source locations. This is possibly due to the fact that stress at depth does not change much for high angle dips when surface waves arrive almost perfectly perpendicular to the fault strike (Fig. S4). Thus, while the Coulomb triggering potential model prefers a near-vertical fault (~90°), the model is unable to distinctly resolve the dip of the EPGF for this study.

We searched all possible dips that might explain triggering of the tremor on the reverse PGJF as well (Fig. 6c). For a fault dip of ~55° on the PGJF, the highest correlation between a computed Love wave 'stressgram' and the tremor envelope occurs. However, this CC value is still lower than when the surface wave stresses of the Chile mainshock are resolved onto a high-angle (>60°) south-dipping EPGF. That is, the triggering potential is greatest for Love wave triggering on a high-angle (>60°) south-dipping EPGF. In addition, it is possible that the fault strike angles we assumed for the stress modeling may not be very accurate. To test this uncertainty in our stress modeling, we calculated CC values by slightly changing the strike from the original assumed values for both faults. We use 0° ± 15° for EPGF (Fig. 6b) and 125° ± 15° for PGJF (Fig. 6d), and in both cases, we observe that the variable strike angles do not change the CC values significantly.

We offer one further note on using the triggering potential for testing fault orientation. In this study, we treat locating the triggered tremor sources and estimation of fault orientation as being independent of each other. However, estimation of fault orientation using the Coulomb triggering potential largely depends on the location of the tremor sources. Therefore, we suggest that future works could consider joint estimation of tremor location and fault orientation when modeling transient stresses that trigger on unknown fault structures.

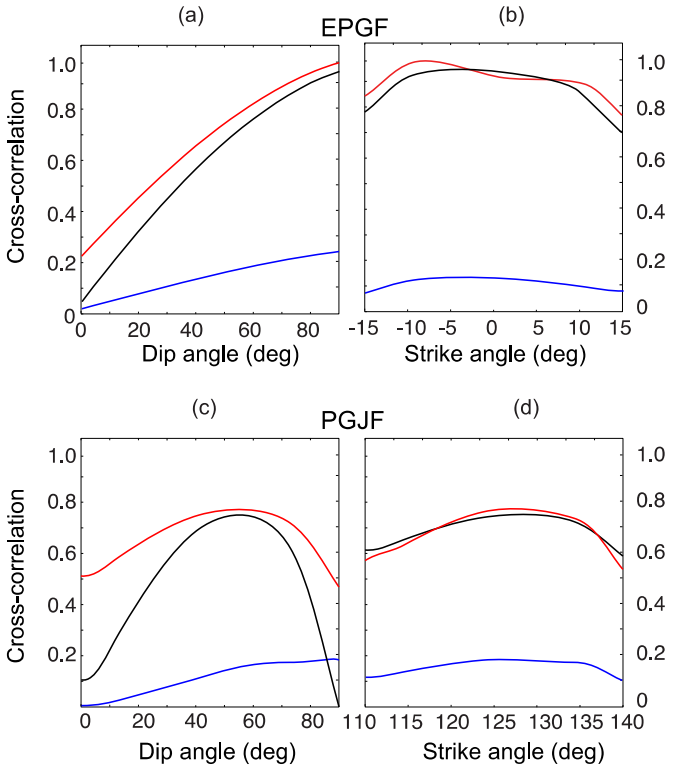

Fig. 6. Cross-correlation values between tremor envelope and Love wave 'stressgram' (see Fig. 5) computed for varied dip and strike angles, source locations, and time windows for the (a–b) Enriquillo–Plantain Garden Fault (EPGF) and (c–d) Petit Goave–Jacmel Fault (PGJF). Black lines = correlation values when the 'stressgram' is computed at the average tremor source location for the entire surface wave window (test #1 in Table 1). Red lines = 'stressgram' computed at the burst #5 location for the entire surface wave window (test #2). Blue lines = only burst #5 location and its window (test #3). Correlation is greatest for a left lateral strike-slip EPGF with high-angle (>60°) dips.

3. Search for triggered aftershock activity

3.1. Aftershock detection

To investigate if aftershock activity of the Haiti mainshock was promoted by transient stress changes generated by the Chile mainshock, we applied a matched filter detection technique (*e.g.*, Peng and Zhao, 2009; Meng et al., 2013) to continuous seismic data from 23 February through 2 March 2010. This technique uses waveforms of known earthquakes as templates for scanning through continuous seismic data in search of similar events, *i.e.* detections are made via cross-correlations over numerous time windows. In this study, we utilized aftershocks detected by the Canadian National Seismograph Network (CNSN) and Douilly et al. (2013) from 23 February through 2 March 2010 as template events. The aftershock catalog of Douilly et al. (2013) does not contain event magnitudes, and so we compared events in their catalog to the CNSN earthquake catalog that provides event magnitudes and used the CNSN magnitude, if available. Not all aftershocks listed in Douilly et al. (2013) are also listed in the CNSN catalog (and vice versa). Nonetheless, we utilized all earthquakes in these catalogs (with and without magnitude) as templates.

For template event location, we assigned the locations of Douilly et al. (2013) where applicable since in that study the *hypoDD* program (Waldhauser and Ellsworth, 2000) was used to relocate aftershocks, making their locations more accurate than those listed in the CNSN catalog. In total, we used 79 known earthquakes as templates for the matched filter detection. Table S3 provides a

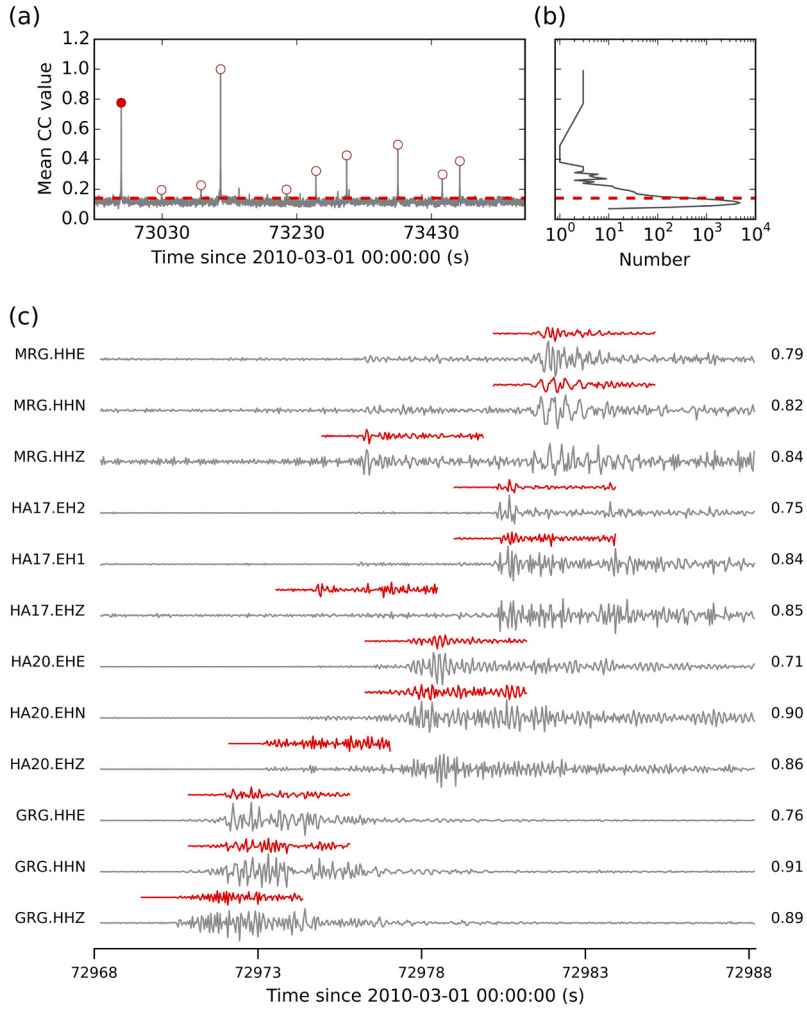

Fig. 7. Example of a Haiti aftershock detected using the matched filter technique. (a) Mean cross-correlation function created from stacking cross-correlation functions across all channels. Dashed red line marks 9 times the median absolute deviation (MAD) of the correlation trace, which is used as a threshold for avoiding false detections. Circles mark detections. (b) Histogram of the mean CC function. (c) Comparisons between continuous (gray) and template waveforms (red) at a few station-channel pairs (*e.g.*, GRG.HHZ) and their corresponding correlation value (marked on the right) for the detection marked as solid red in (a). A CC value of 1 is when a template detects itself (*i.e.*, a self-detection).

summary of the origin time, location, and magnitude (if available) of those templates.

After identifying templates from local earthquake catalogs, we cut the templates from each channel for each day of seismic data that had been filtered to the 2–16 Hz frequency band. Then, each channel's template was cross-correlated with the same channel's 24-hr seismic record from 23 February through 2 March 2010, shifting in time. The highest mean cross-correlation value (CC) across all channels above 9 times the median absolution deviation (MAD) was taken as the CC value for the detected earthquake (*e.g.*, Fig. 7). After detecting earthquakes using the template events, we removed duplicate detections and verified that there were no false detections by examining the waveforms of each detected earthquake. For a more detailed description of how we performed the matched filter detection, please refer to Appendix A.

3.2. Aftershock observations

From 23 February through 2 March 2010, we detected a total of 1,829 earthquakes using templates with and without known magnitude. The magnitude of completeness M_c, which describes the lower magnitude limit the local seismic network can detect, was 1.5 for our detection catalog (Fig. 8b). A M_c of 1.5 is 0.6 less than the CNSN catalog M_c (Fig. S5). Considering only detected events with $M \geq M_c = 1.5$, we observed ~10 times the number of events listed in the CNSN catalog for the same time period using the matched filter technique (Fig. 8a).

Based on the cumulative number of events (Fig. 8a), we considered the possibility that an increase in aftershock activity might have occurred in the first few days following the Chile mainshock, including two M ~ 3 earthquakes that occurred immediately after the *P*-wave of the Chile mainshock (Fig. 2). To examine this further, we first computed the seismicity rate from sliding time windows (*e.g.*, Ziv et al., 2003; Felzer and Brodsky, 2006) using events in our detection catalog with a cutoff magnitude of $M \geq M_c = 1.5$. We observed that the median seismicity rate increased from 63 events day^{-1} before to 78 events day^{-1} after the Chile mainshock (Fig. 8c).

We further tested whether these changes in seismicity rate were significant using the Z value, a simple statistical test of rate change which contrasts the observational time windows before and after an event to the number of event occurrences detected in those time windows. It is known that the Z value is less dependent upon the sample size compared to the β statistical test and is computed as

$$Z = \frac{N_a T_b - N_b T_a}{\sqrt{N_a T_b^2 + N_b T_a^2}} \tag{2}$$

where T_a is the length of the triggering time window, T_b is the length of the background seismicity window, and N_a and N_b are the number of event occurrences in the specified time windows (Marsan and Wyss, 2011). We verified the robustness of the Z value by using different time windows (from 6 to 72 h) and by randomly sampling the background seismicity (*i.e.*, before the Chile mainshock) from our detected catalog 100 times (Fig. 8d). These tests indicate that the increase in seismicity rate following the Chile mainshock is significant ($Z > 2$) when the background window is larger. However, when the cutoff magnitude for the catalog is varied ($1 \leq M \leq 2.5$) and Z values recalculated, the seismicity rate increase following the Chile mainshock is only significant for a cutoff magnitude $M \leq 1.5$ and not for larger cutoff magnitudes (Fig. S6). However, we note that by varying the cutoff magnitude for the Z value tests, we inherently alter our sample size and therefore our significance estimate.

We also tested the significance of Haiti aftershock triggering by examining the spatial distribution of events around the time of the Chile mainshock. We compute Z values for ± 3 days around the Chile mainshock in $0.02^\circ \times 0.02^\circ$ bins over the entire Haiti region at different magnitude thresholds (Fig. S7). With or without a magnitude threshold ($1 \leq M \leq 2.5$), there were fewer triggered ($Z > 2$) areas than non-triggered areas, i.e. 4% or less of active spatial bins experienced a 95% confidence increase in earthquake activity.

4. Discussion and conclusion

In this study, we investigated how seismic waves from the 27 February 2010 *Mw*8.8 Maule, Chile earthquake triggered seismicity around the aftershock zone of the 12 January 2010 *Mw*7.0 Haiti earthquake. We examined seismic data from 25 stations (6 on land, 19 offshore) in search of tremor and Haiti aftershocks possibly induced by the remote Chile earthquake. We identified ~10 tremor bursts triggered instantaneously by the long period surface waves of the Chile mainshock (Fig. 3), the first observation of tremor in the southern Haiti peninsula. The triggered tremor sources radiated in the ~1–10 Hz frequency band (Fig. 2) from just south of the EPGF fault trace but had no clear migration pattern (Fig. 4). Immediately following the Chile earthquake, the Haiti aftershock rate increased slightly in the next few days (Fig. 8), but this increase in aftershock activity depends upon the choice of the cutoff magnitude (Fig. S6), and we, therefore, consider an increase in aftershock activity may have possibly occurred based on the inclusion on small magnitude events in the significance tests.

For the tremor sources, our locations have horizontal errors of ~5 km on average. The location errors are either a result of using a 1D velocity model when 3D velocity variations exist, or it could be due to the fact that a tremor signal may represent several low-frequency earthquakes occurring in rapid succession (*e.g.*, Shelly et al., 2007). If the latter, then the envelope cross-correlation method we used for locating the tremor sources is possibly providing the average location of low-frequency earthquakes that occurred in rapid succession. We note that the depths of the tremor sources are not well resolved, with the exception of tremor burst #5 (Fig. S2), which had the highest amplitude compared to the other triggered tremor (Fig. 3). It is reasonable to assume that the accuracy of the envelope cross-correlation method for locating tremor sources depends somewhat on amplitude. For instance, a known aftershock (starred in Table S3) located with the same envelope cross-correlation method (and seismic stations) and using only its *S*-wave arrival was found to have nearly an identical horizontal and vertical location (Fig. S8) to that of Douilly et al. (2013) who used the *hypoDD* program for source location. Of course, it cannot go without saying that earthquakes, which generally have larger amplitude, also have clear impulsive arrivals (*e.g.*, Fig. 2), which likely makes it easier to resolve their depths.

When the surface wave stresses of the Chile mainshock were resolved onto fault planes parallel to the EPGF and PGJF, we found that the triggered tremor best correlates (Table 2) as a source occurring on the down-dip extension of a high-angle strike-slip EPGF (Figs. 4b and 6), in accordance with the Coulomb failure criterion (Hill, 2012). Field observations and aftershock detections suggest that the EPGF has vertical to high-angle ($>60^\circ$) dip toward the south (Prentice et al., 2010; Douilly et al., 2013), which overlaps with the northern end of the tremor location distribution (Fig. 4). However, we note that others suggest the EPGF could dip to the north (Nettles and Hjörleifsdóttir, 2010). We also checked that the tremor might have occurred on the south-dipping reverse PGJF, but the stress modeling for a tremor source on the PGJF yielded somewhat lower CC values (Table 2). Despite this lower correlation, the tremor sources do coincide well with low shear velocity anomalies along the PGJF (Douilly et al., 2016). Low shear velocity anomalies or high Vp/Vs ratios are used as a means of detecting the presence of fluid and often coincide with tremor locations (*e.g.*, Shelly et al., 2006; Becken et al., 2011). While our tremor locations coincide laterally with a low-velocity anomaly along the PGJF, the low-velocity anomaly occurs at ~10 km depth, which is much shallower than the depths we constrained for the tremor sources (Fig. S2).

Moreover, given the orientation of the studied faults relative to the surface waves direction of propagation, Love waves will cause mainly shear stress changes while Rayleigh waves will cause mainly normal stress changes (Gonzalez-Huizar and Velasco, 2011; Hill, 2012). Thus, in a general approach, we can consider the 'stressgrams' of the Love and Rayleigh waves (Fig. 5) as a proxy to the total shear and normal stress changes, respectively. In addition, given the relatively small amplitude of the Rayleigh wave from the Chile mainshock, and thus, the small contribution of the normal stress changes to the triggering potential, we can consider that the large shear stress changes, caused by the Love waves from the Chile mainshock, were primarily responsible for triggering tremor in Haiti.

Shelly and Johnson (2011) showed that the *M*6.0 Parkfield earthquake (~8 km depth) induced ~1 kPa of static stress changes on the strike-slip San Andreas Fault at depths where tremor occurs (~25 km). Though small, these static stress changes increased tremor activity rates by at most 2 orders of magnitude over a 30-day period in the Parkfield region. Therefore, one may consider the possibility that the 2010 *Mw*7.0 Haiti earthquake may have induced positive static stress changes on the down-dip extension of the EPGF where we assume the triggered tremor occurred in this study. Symithe et al. (2013) estimated that static stress increased by ~20 kPa at about 20 km depth on the EPGF due to the *Mw*7.0 Haiti earthquake, when assuming a dip of 65°S. Given that this static stress change is larger than the dynamic stress changes caused by the Chile mainshock, it is possible that ambient tremor activity was encouraged on the down-dip extension of the EPGF by the 2010 *Mw*7.0 Haiti earthquake. Unfortunately, we cannot substantiate the effect of the Haiti earthquake on tremor activity rates immediately following the mainshock because no research quality stations where in operation at that time. Moreover, while this static stress change is large, it decays quickly with increasing distance from the fault and is unlikely to cause a large static stress change over the entire source area of the tremor.

We also applied the matched filter technique (*e.g.*, Fig. 7) to investigate the possibility that the Chile mainshock induced Haiti aftershock activity. Based on our seismicity rate results, an increase in seismicity could possibly have occurred after the Chile mainshock (Fig. 8). This increase is apparent only when taking into account small magnitude events over the entire study region, with time being the only factor (Fig. S6). In this case, our findings are generally consistent with recent studies that small

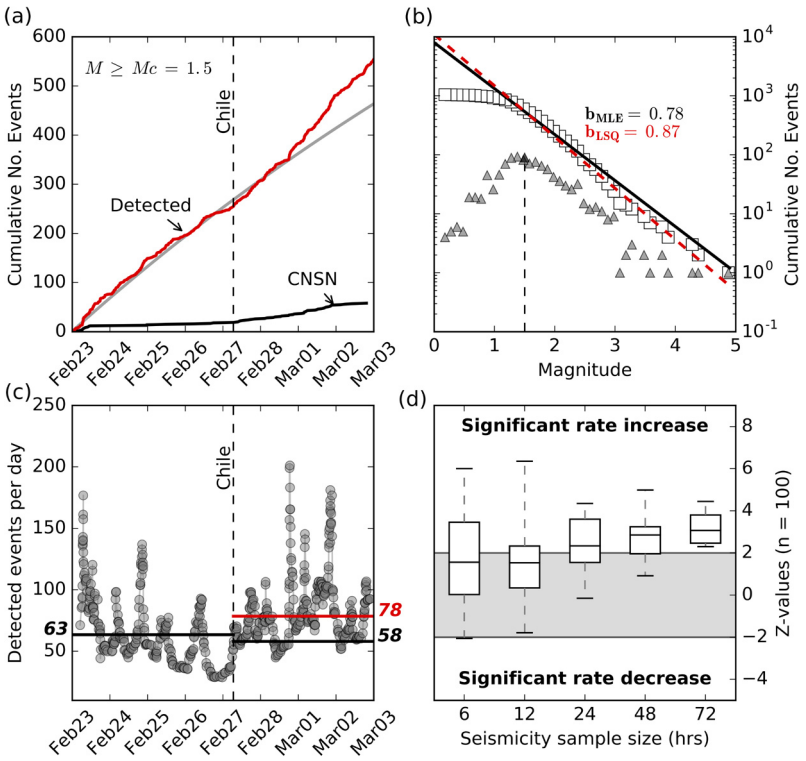

Fig. 8. Summary of aftershock detection and seismicity rates around the time of the Chile mainshock. (a) Comparison of events with $M \geq 1.5$ in CNSN catalog and our detection catalog. Douilly et al. (2013) catalog is excluded here because that catalog does not contain magnitude. Solid gray line marks cumulative number associated with the median detection background rate of 63 events day^{-1}. (b) Gutenberg–Richter relationship $N = 10^{(a-bM)}$ for our detection catalog from February 23 through March 2 (events without magnitude are excluded). Maximum likelihood and least square methods were used for b-value evaluation. (c) Median number of detected events day^{-1} (with $M \geq 1.5$) appears to increase from 63 to 78 after the Chile mainshock. Line showing 58 events day^{-1} marks approximate aftershock rate after the Chile mainshock estimated from Omori decay law with constant productivity K and $p = 1$. (d) Z value distribution for varied background seismicity windows. Median Z value is greater than 2 for larger background window sampling sizes, but Z values were also found to depend upon cutoff magnitude (Fig. S6).

magnitude earthquakes are more easily triggered than larger ones (Parsons et al., 2012). Our findings also partially agree with induced seismicity observations where larger magnitude events are often not present during the early stages of fluid injection (Ellsworth, 2013). However, we did not observe a broad spatial distribution of increase in seismicity across the southern Haiti region even at small magnitudes (Fig. S7) nor does there appear to be any significance in delay of large magnitude ($M > 2.5$) events in the 3 days following the Chile mainshock (Figs. S5–S6). In addition, both the ANSS and CNSN reported the next large earthquakes ($\sim M4$) occurred 3–4 weeks after the Chile mainshock passed through the southern Haiti region.

We note that the Haiti aftershocks decay with time, while we assumed a constant activity rate for the Z value calculation (Fig. 8). Hence, the obtained Z value likely underestimates the true rate changes after accounting for the Omori-law decay. If we assume the Omori-law decay constant $p = 1$ then aftershock rate is $r = Kt^{-1}$, where r is rate, K is productivity, and t is time since the Haiti mainshock. Assuming K is constant for the aftershock sequence and a pre-Chile aftershock rate of 63 events day^{-1} (Fig. 8), the expected number of $M \geq 1.5$ aftershocks 2 days after the Chile mainshock is $\sim$58 events day^{-1}, only a 7% decay from $\sim$63 events day^{-1}. The detected seismicity rate for $M \geq 1.5$ aftershocks after the Chile mainshock is $\sim$78 events day^{-1}, which is a 23% increase from $\sim$58 events day^{-1}. Therefore, there is a small possibility that Haiti aftershock activity increased following the Chile mainshock, but the increase activity is not broadly distributed across the southern Haiti peninsula (Fig. S7). This is generally consistent with recent studies – that tremor may be more easily triggered than microearthquakes both in field (Aiken and Peng, 2014) and laboratory (Bartlow et al., 2012) settings. In general, these findings are attributed to lower effective normal stress (weaker fault "clamping") at tremor depth due to near lithostatic pore pressures (Thomas et al., 2009).

Since the matched filter technique is based on the waveform similarity between a template event and a continuous waveform, the aftershocks we detected likely occurred very near to the location of the template events. Most of these aftershocks occurred on secondary high-angle reverse faults north of the EPGF (Fig. 4b) (Douilly et al., 2013). Most earthquake triggering cases are observed in geothermal/volcanic environments undergoing extensional tectonics (Hill and Prejean, 2015) or near fluid injection sites (van der Elst et al., 2013) and rarely (if at all) within compressional tectonic regimes (Harrington and Brodsky, 2006; Hill, 2015). As shown in Hill (2015), reverse faults are typically further from failure, but one would expect that faults under positive static stress changes generated by a local mainshock would be susceptible to dynamic stress changes as well. However, even the optimally oriented Trois Baies Fault ($\sim$45° dip) which produced aftershocks was not reactivated, statistically speaking, by the $>$10 kPa of dynamic stress generated by the seismic waves of the Chile mainshock (Fig. 5, Fig. 8). One other possible explanation is that at this time in the Haiti mainshock–aftershock sequence larger fault patches had already released their stress and that only small fault patches remained. Such a scenario offers an explanation for the seeming upper magnitude limit and dependency of the Z value statistics on the cutoff magnitude when considering events in the entire aftershock region (Fig. S6).

Regardless of the type of seismic activity induced, investigating remote triggering is important for understanding the fundamental physics of how faults rupture, and there are many remaining questions regarding triggering and fault interaction at the local and

global scale. For example, is there a global aftershock zone that can be influenced by large, distant earthquakes, and does an upper magnitude limit for remotely triggered earthquakes exist (*e.g.*, Johnson et al., 2015)? In addition, where triggered tremor is discovered, does ambient tremor activity also occur there, and if so, what does that ambient tremor activity tell us about large earthquake cycles (*e.g.*, Wech and Creager, 2011)? These directions of research aimed at understanding earthquakes cycles as well as the role of tremor in them are promising for mitigating the effects of future earthquakes.

5. Data and resources

Research groups from Géoazur and the Institut Français de Recherche pour l'Exploitation de la Mer (IFREMER) installed temporary short period and broadband ocean bottom seismometers, which have four components including a hydrophone. The Institut de Physique du Globe de Paris (IPGP) also temporarily deployed four 3-component broadband seismometers near the EPGF trace, and the Natural Resources Canada (NRCan) agency installed 2 broadband seismometers near Jacmel (station JAKH) and Port-au-Prince (station PAPH). Seismic data from the Géoazur and IFREMER research groups are not openly accessible. However, seismic data recorded at stations JAKH and PAPH of the CN network (NRCan agency) are openly accessible via the IRIS Data Management Center (http://www.iris.edu/dms/dmc/). In addition, seismic data collected by IPGP (stations PEM, MRG, PTG, and GRG of the YB network) are openly accessible via the International Federation of Digital Seismograph Networks webservices (http://portal.resif.fr/?FDSN-webservices). Chile aftershock information shown in Fig. 3 is freely accessible at the North California Earthquake Data Center (www.ncedc.org). The seismic travel time *TauP* program is available at http://www.seis.sc.edu/taup/ (last accessed July 5, 2016). For a more detailed summary of the station information, please refer to Table 1 of Douilly et al. (2013). Figs. 1, 3, 4, 7, 8 were made using Python 3.4.3 (open source). Figs. 2, 5, 6 were made using MatLab (proprietary).

Acknowledgements

We thank Xiaofeng Meng for his guidance with performing the matched filter detection. We also thank Tom Parsons and Mike Brudzinski for useful comments on this manuscript. This material is based upon work supported by the National Science Foundation Graduate Research Fellowship for C.A. under Grant No. DGE-1148903 and two ARCS Foundation awards. Z.P. is supported by National Science Foundation CAREER Grant EAR-0956051. H. G-H. is supported by Southern California Earthquake Center (SCEC). SCEC is funded by National Science Foundation cooperative agreement EAR-1033462 and U.S. Geological Survey cooperative agreement G12AC20038.

Appendix A. Matched filter detection

We performed the matched filter detection over several days of seismic data. First, we applied a 2–16 Hz band-pass filter to the continuous waveforms, *i.e.* from 23 February through 2 March 2010. Next, we changed the sampling rate of all the continuous waveforms to be the same (50 Hz) for ease of cross-correlation computation. The template events (Table S3) were then cut from each channel of the continuous seismic data 30 s before and 120 s after the origin time of the template. The *P*- and *S*-wave arrivals of the template events were used as markers for computing the signal-to-noise ratio (SNR) on the vertical and horizontal components, respectively. For each component, the signal window is from 1 s before to 5 s after the corresponding body wave arrival, while the noise window is from 7 s before to 1 s before the *P*-wave arrival. The signal window for each body wave phase is also used in the cross-correlation of the template with the continuous data.

We require that at least 9 channels have SNR > 5 for a single template to perform the cross-correlation between the template event and continuous seismic data. If this criterion is met, then each template on each channel was cross-correlated with the corresponding channel for each continuous day seismic recording, recomputing the cross-correlation value (CC) by sliding every time sample. The CC value for each channel for a single template was then stacked and averaged, and only events above 9 times the median absolute deviation (MAD) of the CC trace were kept to insure no false detections. Duplicate detections were also removed, and only detections with the highest CC value were kept.

We estimated the magnitude of detected earthquakes by computing the amplitude ratio between the detected event and template event with known magnitude (Table S3). The amplitude ratio is computed for all channels and the median amplitude ratio for a single detected event is used for magnitude estimation. The magnitude is computed as

$$M_d = M_k + \log_{10}(AR) \tag{A.1}$$

where M_d is detected event magnitude, M_k is known template event magnitude, and AR is the amplitude ratio computed as described above. We did not compute the magnitude of events detected with a template event without known magnitude. Fig. S9 shows all detections made with the matched filter technique without regard to magnitude and those with magnitude $\geq$1.5. Fig. S10 shows earthquakes detections made on a waveform envelope from station JAKH $\pm$ 2 h around the Chile mainshock.

Appendix B. Supplementary material

Supplementary material related to this article can be found online at http://dx.doi.org/10.1016/j.epsl.2016.09.023.

References

Aiken, C., Peng, Z., 2014. Dynamic triggering of microearthquakes in three geothermal regions of California. J. Geophys. Res. 119, 6992–7009. http://dx.doi.org/10.1002/2014JB011218.

Aiken, C., Peng, Z., Chao, K., 2013. Tremors along the Queen Charlotte Margin triggered by large teleseismic earthquakes. Geophys. Res. Lett. 40, 829–834. http://dx.doi.org/10.1002/grl.50220.

Aiken, C., Zimmerman, J.P., Peng, Z., Walter, J.I., 2015. Triggered seismic events along the Eastern Denali Fault in northwest Canada following the 2012 *Mw*7.8 Haida Gwaii, 2013 *Mw*7.5 Craig, and two *Mw* > 8.5 teleseismic earthquakes. Bull. Seismol. Soc. Am. 105 (2B), 1165–1177. http://dx.doi.org/10.1785/0120140156.

Bakun, W.H., Flores, C.H., ten Brink, U.S., 2012. Significant earthquakes on the enriquillo fault system, Hispaniola, 1500–2010: implications for seismic hazard. Bull. Seismol. Soc. Am. 102 (1), 18–30. http://dx.doi.org/10.1785/0120110077.

Bartlow, N.M., Lockner, D.A., Beeler, N.M., 2012. Laboratory triggering of stick-slip events by oscillatory loading in the presence of pore fluid with implications for physics of tectonic tremor. J. Geophys. Res. 117, B11411. http://dx.doi.org/10.1029/2012JB009452.

Becken, M., Ritter, O., Bedrosian, P.A., Weckmann, U., 2011. Correlation between deep fluids, tremor and creep along the central San Andreas fault. Nature 480, 87–90. http://dx.doi.org/10.1038/nature10609.

Beroza, G.C., Ide, S., 2011. Slow earthquakes and nonvolcanic tremor. Annu. Rev. Earth Planet. Sci. 39, 271–296. http://dx.doi.org/10.1146/annurev-earth-040809-152531.

Brodsky, E.E., Prejean, S.G., 2005. New constraints on mechanisms of remotely triggered seismicity at Long Valley Caldera. J. Geophys. Res. 110, B04302. http://dx.doi.org/10.1029/2004JB003211.

Brodsky, E.E., Roeloffs, E., Woodcock, D., Gall, I., Manga, M., 2003. A mechanism for sustained groundwater pressure changes induced by distant earthquakes. J. Geophys. Res. 108 (B8), 2390. http://dx.doi.org/10.1029/2002JB002321.

Brodsky, E.E., van der Elst, N.J., 2014. The uses of dynamic triggering. Annu. Rev. Earth Planet. Sci. 42, 317–339. http://dx.doi.org/10.1146/annurev-earth-060313-054648.

Calais, E., Freed, A., Mattioli, G., Amelung, F., Jónsson, S., Jansma, P., Hong, S-H., Dixon, T., Prépetit, C., Momplaisir, R., 2010. Transpressional rupture of an unmapped fault during the 2010, Haiti earthquake. Nat. Geosci. 3, 794–799. http://dx.doi.org/10.1038/ngeo992.

Chao, K., Obara, K., 2016. Triggered tectonic tremor in various types of fault systems of Japan following the 2012 *Mw*8.6 Sumatra earthquake. J. Geophys. Res. 120, 170–187. http://dx.doi.org/10.1002/2015JB012566.

Chao, K., Peng, Z., Gonzalez-Huizar, H., Aiken, C., Enescu, B., Kao, H., Velasco, A.A., Obara, K., Matsuzawa, T., 2013. A global search for triggered tremor following the 2011 *Mw*9.0 Tohoku earthquake. Bull. Seismol. Soc. Am. 103 (2B), 1551–1571. http://dx.doi.org/10.1785/0120120171.

Douilly, R., Ellsworth, W.L., Kissling, E., Freed, A.M., Deschamps, A., Mercier de Lepinay, B., 2016. 3D velocity structure in southern Haiti from local earthquake tomography. J. Geophys. Res., Solid Earth, revised and resubmitted.

Douilly, R., Haase, J.S., Ellsworth, W.L., Bouin, M.P., Calais, E., Symithe, S., Armbruster, J.G., Mercier de Lépinay, B., Deschamps, A., Mildor, S.L., Meremonte, M., Hough, S., 2013. Crustal structure and fault geometry of the 2010 Haiti earthquake from temporary seismometer deployments. Bull. Seismol. Soc. Am. 103 (4), 2305–2325. http://dx.doi.org/10.1785/0120120303.

Ellsworth, W.L., 2013. Injection-induced earthquakes. Science 341, 1225942. http://dx.doi.org/10.1126/science.1225942.

Felzer, K., Brodsky, E.E., 2006. Decay of aftershock density with distance indicates triggering by dynamic stress. Nature 441, 735–738. http://dx.doi.org/10.1038/nature04799.

Fry, B., Chao, K., Bannister, S., Peng, Z., 2011. Deep tremor beneath the Hikurangi margin in New Zealand triggered by the 2010 *Mw*8.8 Chile earthquake. Geophys. Res. Lett. 38, L15306. http://dx.doi.org/10.1029/2011GL048319.

Gomberg, J., Prejean, S., 2013. Triggered tremor sweet spots in Alaska. J. Geophys. Res. 118, 6203–6218. http://dx.doi.org/10.1002/2013JB010273.

Gonzalez-Huizar, H., Velasco, A.A., 2011. Dynamic triggering: stress modeling and a case study. J. Geophys. Res. 116, B02304. http://dx.doi.org/10.1029/2009JB007000.

Harrington, R.M., Brodsky, E.E., 2006. The absence of remotely triggered seismicity in Japan. Bull. Seismol. Soc. Am. 96 (3), 871–878. http://dx.doi.org/10.1785/0120050076.

Hill, D.P., 2012. Surface wave potential for triggering tectonic (non-volcanic) tremor – corrected. Bull. Seismol. Soc. Am. 102 (6), 2337–2355. http://dx.doi.org/10.1785/0120120086.

Hill, D.P., 2015. On the sensitivity of transtensional versus transpressional tectonic regimes to remote dynamic triggering by Coulomb failure. Bull. Seismol. Soc. Am. 105 (3), 1339–1348. http://dx.doi.org/10.1785/0120140292.

Hill, D.P., Peng, Z., Shelly, D.R., Aiken, C., 2013. *S*-wave triggering of tremor beneath the Parkfield, California, section of the San Andreas fault by the 2011 Tohoku, Japan, earthquake: observations and theory. Bull. Seismol. Soc. Am. 103 (2B), 1541–1550. http://dx.doi.org/10.1785/0120120114.

Hill, D.P., Prejean, S.G., 2015. Dynamic triggering. In: Schubert, G. (Ed.), Treatise on Geophysics, 2nd edition. In: Kanamori, H. (Ed.), Earthquake Seismology, vol. 4. Elsevier, Amsterdam. Chapter 8.

Hough, S.E., Seeber, L., Ambruster, J.G., 2003. Intraplate triggered earthquakes: observations and interpretation. Bull. Seismol. Soc. Am. 93 (5), 2212–2221. http://dx.doi.org/10.1785/0120020055.

Houston, H., 2015. Low friction and fault weakening revealed by rising sensitivity of tremor to tidal stress. Nat. Geosci. 8, 409–415. http://dx.doi.org/10.1038/ngeo2419.

Jiang, T., Peng, Z., Wang, W., Chen, Q.-F., 2010. Remotely triggered seismicity in continental China by the 2008 *Mw*7.9 Wenchuan earthquake. Bull. Seismol. Soc. Am. 100, 5274–5289. http://dx.doi.org/10.1785/0120090286.

Johnson, C.W., Bürgmann, R., Pollitz, F.F., 2015. Rare dynamic triggering of remote $M \geq 5.5$ earthquakes from global catalog analysis. J. Geophys. Res. 130 (3), 1748–1761. http://dx.doi.org/10.1002/2014JB011788.

Kilb, D., Blasi, G., Anderson, J., Brune, J., Peng, Z., Vernon, F., 2012. Listen, watch, learn: SeisSound video products. Seismol. Res. Lett. 83 (2), 281–286. http://dx.doi.org/10.1785/gssrl.83.2.287.

Marsan, D., Wyss, M., 2011. Seismicity rate changes. Community Online Resour. Stat. Seism. Anal. http://dx.doi.org/10.5078/corssa-25837590. Available at http://www.corssa.org.

Meng, X., Peng, Z., Hardebeck, J., 2013. Seismicity around Parkfield correlates with static shear stress changes following the 2003 *Mw*6.5 San Simeon earthquake. J. Geophys. Res. 118 (7), 3576–3591. http://dx.doi.org/10.1002/jgrb.50271.

Mercier de Lépinay, B., Deschamps, A., Klingelhoefer, F., Mazabraud, Y., Delouis, B., Clouard, V., Hello, Y., Crozon, J., Marcaillow, B., Graindorge, D., Vallée, M., Perrot, J., Bouin, M-P., Saurel, J-M., Charvis, P., St-Louis, M., 2011. The 2010 Haiti earthquake: a complex fault pattern constrained by seismologic and tectonic observations. Geophys. Res. Lett. 38, L22305. http://dx.doi.org/10.1029/2011GL049799.

Nettles, M., Hjörleifsdóttir, V., 2010. Earthquake source parameters for the 2010 January Haiti mainshock and aftershock sequence. Geophys. J. Int. 183, 375–380. http://dx.doi.org/10.1111/j.1365-246X.2010.04732.x.

Obara, K., 2002. Nonvolcanic deep tremor associated with subduction in southwest Japan. Science 296, 1679–1681. http://dx.doi.org/10.1126/science.1070378.

Parsons, T., Kaven, J.O., Velasco, A.A., Gonzalez-Huizar, H., 2012. Unraveling the apparent magnitude threshold of remote earthquake triggering using full wavefield surface wave simulation. Geochem. Geophys. Geosyst. 13, Q06016. http://dx.doi.org/10.1029/2012GC004164.

Peng, Z., Aiken, C., Kilb, D., Shelly, D., Enescu, B., 2012. Listening to the 2011 magnitude 9.0 Tohoku-Oki, Japan earthquake. Seismol. Res. Lett. 83 (2), 287–293. http://dx.doi.org/10.1785/gssrl.83.2.287.

Peng, Z., Gomberg, J., 2010. An integrative perspective of couple seismic and aseismic slow slip phenomena. Nat. Geosci. 3, 599–607. http://dx.doi.org/10.1038/ngeo940.

Peng, Z., Gonzalez-Huizar, H., Chao, K., Aiken, C., Moreno, B., Armstrong, G., 2013. Tectonic tremor beneath Cuba triggered by the *Mw*8.8 Maule and *Mw*9.0 Tohoku-Oki earthquakes. Bull. Seismol. Soc. Am. 103 (1), 595–600. http://dx.doi.org/10.1785/0120120253.

Peng, Z., Shelly, D.R., Ellsworth, W.L., 2015. Delayed dynamic triggering of deep tremor along the Parkfield–Cholame section of the San Andreas Fault following the 2014 M6.0 South Napa earthquake. Geophys. Res. Lett. 42 (19), 7916–7922. http://dx.doi.org/10.1002/2015GL065277.

Peng, Z., Walter, J., Aster, R., Nyblade, A., Wiens, D., Anandakrishnan, S., 2014. Antarctic icequakes triggered by the 2010 Maule earthquake in Chile. Nat. Geosci. 7, 677–681. http://dx.doi.org/10.1038/NGEO2212.

Peng, Z., Wu, C., Aiken, C., 2011. Delayed triggering of microearthquakes by multiple surface waves circling the Earth. Geophys. Res. Lett. 38, L04306. http://dx.doi.org/10.1029/2010GL046373.

Peng, Z., Zhao, P., 2009. Migration of early aftershocks following the 2004 Parkfield earthquake. Nat. Geosci. 2, 877–881. http://dx.doi.org/10.1038/ngeo697.

Prejean, S.G., Hill, D.P., Brodsky, E.E., Hough, S.E., Johnston, M.J.S., Malone, S.D., Oppenheimer, D.H., Pitt, A.M., Richards-Dinger, K.B., 2004. Remotely triggered seismicity on the United States west coast following the *Mw*7.9 Denali Fault earthquake. Bull. Seismol. Soc. Am. 94 (6B), S348–S359. http://dx.doi.org/10.1785/0120040610.

Prentice, C.S., Mann, P., Crone, A.J., Gold, R.D., Hudnut, K.W., Briggs, R.W., Koehler, R.D., Jean, P., 2010. Seismic hazard of the Enriquillo–Plantain Garden fault in Haiti inferred from paleoseismology. Nat. Geosci. 3, 789–793. http://dx.doi.org/10.1038/ngeo991.

Shelly, D.R., Beroza, G., Ide, S., Nakamula, S., 2006. Low-frequency earthquakes in Shikoku, Japan, and their relationship to episodic tremor and slip. Nature 442, 188–191. http://dx.doi.org/10.1038/nature04931.

Shelly, D.R., Ellsworth, W.L., Ryberg, T., Haberland, C., Fuis, G.S., Murphy, J., Nadeau, R.M., Bűrgmann, R., 2009. Precise location of San Andreas Fault tremors near Cholame, California using seismometer clusters: slip on the deep extension of the fault? Geophys. Res. Lett. 36, L01303. http://dx.doi.org/10.1029/2008GL036367.

Shelly, D.R., Johnson, K.M., 2011. Tremor reveals stress shadowing, deep postseismic creep, and depth-dependent slip recurrence on the lower-crustal San Andreas fault near Parkfield. Geophys. Res. Lett. 38, L13312. http://dx.doi.org/10.1029/2011GL047863.

Shelly, D.R., Beroza, G.C., Ide, S., 2007. Non-volcanic tremor and low frequency earthquake swarms. Nature 446, 305–307. http://dx.doi.org/10.1038/nature05666.

Symithe, S.J., Calais, E., Haase, J.S., Freed, A.M., Douilly, R., 2013. Coseismic slip distribution of the 2010 M7.0 Haiti earthquake and resulting stress changes on regional faults. Bull. Seismol. Soc. Am. 103 (4), 2326–2343. http://dx.doi.org/10.1785/0120120306.

Thomas, A., Nadeau, R.M., Bürgmann, R., 2009. Tremor-tide correlations and near-lithostatic pore pressure on the deep San Andreas fault. Nature 462, 1048–1051. http://dx.doi.org/10.1038/nature08654.

Toda, S., Lin, J., Stein, R.S., 2011. Using the 2011 $M = 9.0$ Tohoku earthquake to test the Coulomb stress triggering hypothesis and to calculate faults brought closer to failure. Earth Planets Space 63, 725–730. http://dx.doi.org/10.5047/eps.2011.05.010.

van der Elst, N.J., Savage, H.M., Keranen, K.M., Abers, G.A., 2013. Enhanced remote earthquake triggering at fluid-injection sites in the Midwestern United States. Science 341 (6142), 164–167. http://dx.doi.org/10.1126/science.1238948.

Velasco, A.A., Hernandez, S., Parsons, T., Pankow, K., 2008. Global ubiquity of dynamic earthquake triggering. Nat. Geosci. 1, 375–379. http://dx.doi.org/10.1038/ngeo204.

Waldhauser, F., Ellsworth, W.L., 2000. A double-difference earthquake location algorithm: method and application to the northern Hayward fault. Bull. Seismol. Soc. Am. 90, 1353–1368. http://dx.doi.org/10.1785/0120000006.

Wech, Creager, 2011. A continuum of stress, strength and slip in the Cascadia subduction zone. Nat. Geosci. 4, 624–628. http://dx.doi.org/10.1038/ngeo1215.

Zigone, D., Rivet, D., Radiguet, M., Campillo, M., Voisin, C., Cotte, N., Walpersdorf, A., Shapiro, N., Cougoulat, G., Roux, P., Kostoglodov, V., Husker, A., Payero, J.S., 2012. Triggering of tremors and slow slip event in Guerrero, Mexico, by the 2010 *Mw*8.8 Maule, Chile, earthquake. J. Geophys. Res. 117 (B9), B09304. http://dx.doi.org/10.1029/2012JB009160.

Ziv, A., Rubin, A.M., Kilb, D., 2003. Spatiotemporal analyses of earthquake productivity and size distribution: observations and simulations. Bull. Seismol. Soc. Am. 93 (5), 2069–2081. http://dx.doi.org/10.1785/0120020117.